MATERIALS SCIENCE

Hollow metal halide perovskite nanocrystals with efficient blue emissions

Michael Worku[1], Yu Tian[1]*, Chenkun Zhou[2], Haoran Lin[3], Maya Chaaban[3], Liang-jin Xu[3], Qingquan He[3], Drake Beery[3], Yan Zhou[3], Xinsong Lin[3], Yi-feng Su[4], Yan Xin[4], Biwu Ma[1,2,3]†

Metal halide perovskite nanocrystals (NCs) have emerged as new-generation light-emitting materials with narrow emissions and high photoluminescence quantum efficiencies (PLQEs). Various types of perovskite NCs, e.g., platelets, wires, and cubes, have been discovered to exhibit tunable emissions across the whole visible spectrum. Despite remarkable advances in the field of perovskite NCs, many nanostructures in inorganic NCs have not yet been realized in metal halide perovskites, and producing highly efficient blue-emitting perovskite NCs remains challenging and of great interest. Here, we report the discovery of highly efficient blue-emitting cesium lead bromide (CsPbBr$_3$) perovskite hollow NCs. By facile solution processing of CsPbBr$_3$ precursor solution containing ethylenediammonium bromide and sodium bromide, in situ formation of hollow CsPbBr$_3$ NCs with controlled particle and pore sizes is realized. Synthetic control of hollow nanostructures with quantum confinement effect results in color tuning of CsPbBr$_3$ NCs from green to blue, with high PLQEs of up to 81%.

INTRODUCTION

Metal halide perovskite nanocrystals (NCs) have received great attention as an emerging class of light-emitting materials for their narrow emissions, exceptional photoluminescence quantum efficiencies (PLQEs), and color tunability (1–4). Various approaches have recently been developed to achieve synthetic control of the composition, size, and shape of perovskite NCs to obtain emissions covering the whole visible spectrum, from deep blue to near-infrared (5–14). For instance, by manipulating the quantum size effect, the emission of CsPbBr$_3$ NCs can be tuned from green for NCs with sizes larger than the exciton bohr radius (~7 nm) to deep blue for quantum dots, nanowires, and nanoplatelets with strong quantum confinement (15–20). Several recent studies have demonstrated NC size control within the quantum confinement regime by introducing organic salts (21), controlling the acid-base environment (22), varying Pb-to-halide ratio (23), etc. (24). Although highly efficient perovskite NCs can be synthesized using colloidal methods, preserving the high PLQEs during transfer of colloidal NCs to thin films for device integration has been challenging (3). On the other hand, in situ formation of highly efficient perovskite NCs is not trivial either, because of the limited control on particle size, monodispersity, and surface passivation. This is even more relevant in blue-emitting perovskite NCs, which are generally in the size range of 4 to 6 nm for CsPbBr$_3$ and thus have high surface area–to–volume ratios that readily lead to high surface defect density and low PLQEs.

Hollow NCs, nanostructures with pores, provide an additional degree of freedom to exploit the quantum size effect by controlling pore and grain sizes. Several classes of hollow NCs have previously been reported, e.g., metal chalcogenides (25, 26), metal oxides (27, 28), and metal nanoparticles (29), with applications in catalysis and energy storage. To the best of our knowledge, hollow metal halide perovskite NCs have not yet been discovered. Here, we report an approach to achieving highly efficient blue emissions from CsPbBr$_3$ perovskite NCs by creating hollow nanostructures with controlled sizes. By spin-casting a mixture solution containing cesium bromide (CsBr), lead bromide (PbBr$_2$), ethylenediammonium bromide [(H$_3$N(CH$_2$)$_2$NH$_3$)Br$_2$], and sodium bromide (NaBr), in situ formation of hollow CsPbBr$_3$ perovskite NCs was achieved. It was found that [NH$_3$(CH$_2$)$_2$NH$_3$]$^{2+}$ (EDA^{2+}) cations act as both surface passivation ligands and A-site cations that lead to the formation of randomly oriented Pb^{2+} vacancies. The presence of Na$^+$ along with EDA^{2+} cations produces hollow nanostructures. By carefully controlling the EDABr$_2$ and NaBr content, size tuning of pore and grain radii of hollow CsPbBr$_3$ perovskite NCs was achieved, resulting in emission color tuning from green (525 nm) to blue (459 nm) with high PLQEs of up to 81%. Our work introduces a unique nanostructure to the family of metal halide perovskites, showing once again their exceptional structural versatility. The hollow perovskite NCs with tunable optical and electronic properties may have potential applications in various optoelectronic applications, for instance, blue light-emitting diodes.

RESULTS

The schematic diagram of a one-step spin-casting process for the preparation of metal halide perovskite thin films is shown in Fig. 1A. Briefly, metal halide perovskite precursors (CsBr and PbBr$_2$) mixed with EDABr$_2$ and NaBr at controlled ratios were spun cast on glass substrates, followed by low-temperature thermal annealing at around 100°C (see experimental details in Materials and Methods). By fixing the concentration of NaBr to 3 mole percent (mol %) with respect to the perovskite precursors and varying the molar ratio of EDABr$_2$ (from 0 to 1.2 with respect to the perovskite precursors), uniform and smooth thin films were produced as evidenced by the atomic force microscopy (AFM) images (fig. S1, A to F). The thickness of these thin films was measured to be 42 ± 8 nm (fig. S2). The thin films were transparent under ambient light but displayed green and blue emissions under UV irradiation (Fig. 1B). The photophysical properties of the thin films were investigated via ultraviolet-visible

[1]Materials Science and Engineering Program, Florida State University, Tallahassee, FL 32306, USA. [2]Chemical and Biomedical Engineering, FAMU-FSU College of Engineering, Florida State University, Tallahassee, FL 32310, USA. [3]Department of Chemistry and Biochemistry, Florida State University, Tallahassee, FL 32306, USA. [4]National High Magnetic Field Laboratory, Florida State University, Tallahassee, FL 32310, USA.
*Present address: Global Solar Energy, Tucson, AZ 85747, USA.
†Corresponding author. Email: bma@fsu.edu
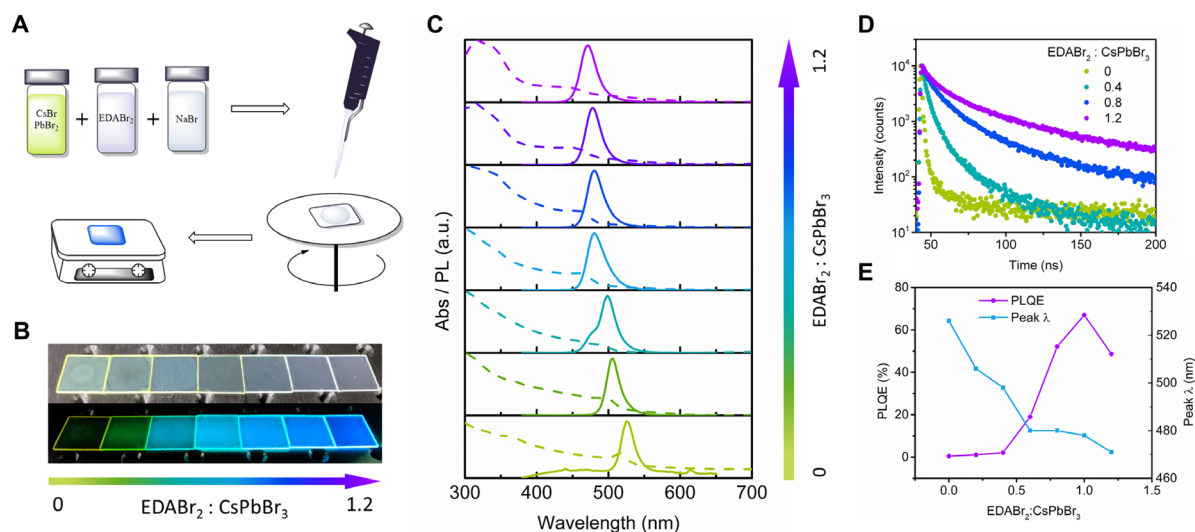
Fig. 1. Processing and photophysical properties of CsPbBr₃ thin films containing 3 mol % NaBr and varying concentrations of EDABr₂. (**A**) A schematic showing the one-step spin coating followed by low-temperature thermal annealing. (**B**) Thin films with various concentrations of EDABr₂ under ambient light (top) and ultraviolet (UV) irradiation (bottom). (Photo credit: M.W., Materials Science and Engineering Program, Florida State University.) (**C**) Photoluminescence (PL) and absorption spectra, (**D**) time-resolved PL (TRPL) decay curves, and (**E**) PLQE and emission peak wavelength of thin films with EDABr₂ molar ratio varying from 0 to 1.2 with respect to the perovskite precursors. a.u., arbitrary units.

(UV-vis) absorption, steady-state and time-resolved photoluminescence (TRPL) spectroscopy, and PLQE measurements. The absorption onset and the PL emission peaks were steadily shifted to lower wavelengths with the increase of the EDABr₂ concentration, while keeping the NaBr content constant (Fig. 1C). This blue shift of emission spectra was also associated with a pronounced increase in the PL decay lifetimes (Fig. 1D and table S1), indicating the role of EDA²⁺ cations in surface defect passivation (*30*). The defect passivation is further supported by PLQE measurements, where samples containing increasing amounts of EDABr₂ showed a steep increase (Fig. 1E), with a peak PLQE of 72% at 478 nm for the sample with 1:1 ratio of EDABr₂ to the perovskite precursors.

To better understand the effects of NaBr and EDABr₂ on the photophysical properties of perovskite thin films, we systemically adjusted the concentration of NaBr with and without the presence of EDABr₂, and vice versa. Changing the NaBr content within the precursor solution (while keeping the concentration of EDABr₂ constant at 1:1 ratio with respect to the perovskite precursors) also afforded emission color tuning, from 498 nm for the sample without NaBr to 459 nm for that containing 4 mol % of NaBr (fig. S3A). However, the PLQEs steadily declined with the increase of NaBr concentration (table S2). Controlling the content of NaBr without the presence of EDABr₂, however, had little to no effect on the PL spectrum and PLQE (fig. S4A). These results suggested that NaBr did not play a passivation role in the thin films. Moreover, by controlling the EDABr₂ content without the presence of NaBr, limited color tuning was achieved, with the blue shift saturating at around 498 nm (fig. S4B). To reveal the structure-property relationships and understand the roles of Na⁺ and EDA²⁺ cations in these systems, we investigated four representative samples in detail, whose compositions and photophysical properties are summarized in Table 1. The sample CsPbBr₃ was prepared from the solution containing perovskite precursors without the addition of NaBr and EDABr₂, the sample CsPbBr₃-Na was prepared from the solution containing perovskite precursors and 3 mol % NaBr, the

sample EDA5 was prepared from the solution containing perovskite precursors and EDABr₂ at 1:1 ratio, and the sample EDA5-Na was prepared from the solution containing perovskite precursors and EDABr₂ at 1:1 ratio and 3 mol % NaBr.

The structural properties of the four samples were investigated by selected-area electron diffraction (SAED) and x-ray powder diffraction (XRD) (Fig. 2, A and B). The sample CsPbBr₃ was identified to have an orthorhombic phase (space group *Pnma*) and the diffraction peaks were indexed accordingly. Apart from small peak shifts (Fig. 2, C and D), the other three samples displayed the same diffraction patterns without any sign of low-dimensional or nonperovskite phases, indicating the formation of a three-dimensional (3D) perovskite structure. The shifts of the diffraction peaks can be ascribed to unit cell contraction or expansion. For the sample CsPbBr₃-Na, slight shifts to higher diffraction angles were observed [$\Delta 2\theta \approx 0.022°$ for the (121) and $\approx 0.054°$ for the (202) planes], which was expected as the incorporation of small Na⁺ cations (ionic radius of 116 pm) at the A-site could lead to unit cell contraction (*31*). This lattice contraction was further confirmed by XPS, which showed a shift of the Pb 4f and Br 3d photoelectron spectra to higher binding energies in comparison to the control sample (Fig. 2, E and F). This indicates an increased Pb-Br interaction as a result of reduced bond length. In contrast, the diffraction peaks for the samples EDA5 and EDA5-Na displayed small shifts to lower 2θ as a result of unit cell expansion. This shift of diffraction peaks could be well explained to result from the incorporation of large EDA²⁺ cations [ionic radius, 333 pm (*32*)] within the 3D perovskite structure, which has previously been shown in other halide perovskites (*32–36*). Previous reports had proposed lattice strain caused by Pb-X (X = Cl, Br, I) bond elongation (*35*) and the formation of a hollow 3D structure (*32*) as mechanisms to explain lattice expansion upon the incorporation of large organic cations. Moreover, because the valence band maximum of ABX₃-type 3D halide perovskites is an antibonding hybrid state of the metal s and halide p orbitals, reduced interaction of the B²⁺ and X⁻ ions, due to

Table 1. Composition and photophysical properties of representative thin-film samples. λ_{em} is the wavelength at the emission maxima, ϕ is the PLQE, and τ_{avg} is the average PL lifetime. FWHM, full width at half maximum.

| Sample	Composition ($CsPbBr_3:EDABr_2:NaBr$)	λ_{em} (nm)	FWHM (nm)	ϕ (%)	τ_{avg} (ns)
$CsPbBr_3$	1:0:0	525	23	0.5	14
$CsPbBr_3$-Na	1:0:0.03	525	23	0.5	18
EDA5	1:1:0	498	22	81.5	200
EDA5-Na	1:1:0.03	478	24	72	150
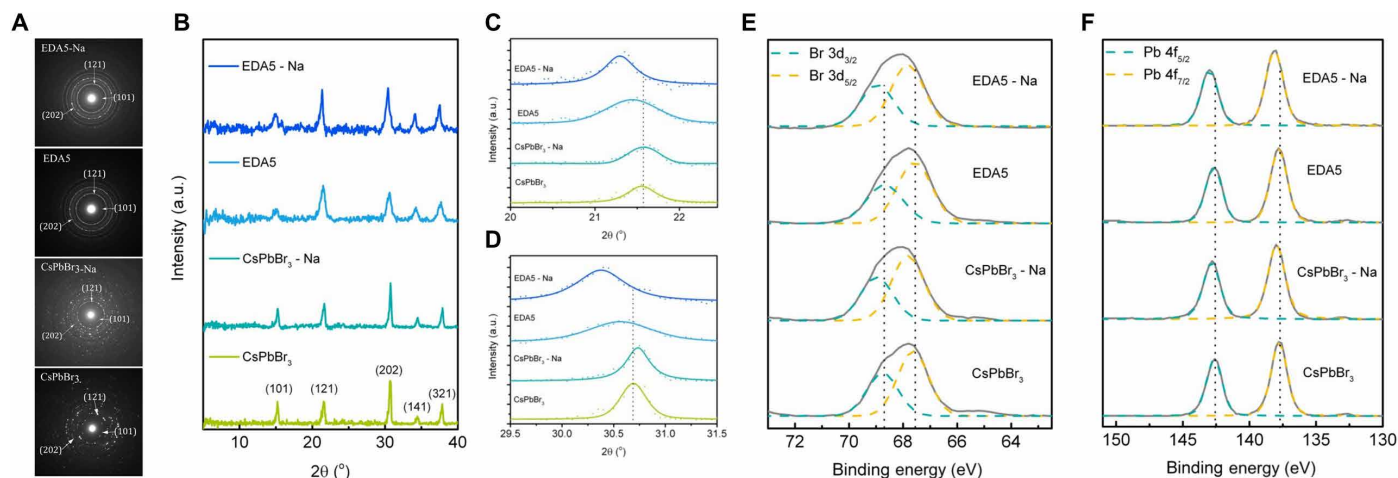
Fig. 2. Structural and surface characterization of thin films. (**A**) SAED patterns of thin films. (**B**) XRD patterns of thin films. (**C**) Pseudo-Voight peak fitting of the diffraction peaks for the (121) and (**D**) (202) crystallographic planes of thin films. Photoelectron spectra from x-ray photoelectron spectroscopy (XPS) and Gaussian peak fitting for (**E**) Br 3d and (**F**) Pb 4f core levels.

either bond elongation or discontinuities, would lead to energy bandgap increase (37).

XPS was used to probe changes of the Pb-Br interactions in the samples EDA5 and EDA5-Na. Lattice expansion caused by Pb—Br bond elongation would shift the Pb 4f and Br 3d photoelectron spectra to lower binding energies (38, 39) without affecting Br/Pb ratio. In contrast, a hollow structure with Pb^{2+} vacancies should display higher Br/Pb ratio but little to no change in binding energies of the core levels. Pb 4f and Br 3d photoelectron spectra for EDA5 show no shift compared to those from $CsPbBr_3$ (Fig. 2, E and F). Moreover, quantitative analysis of the XPS spectra showed that Br/Pb ratio increased substantially with the incorporation of EDA^{2+} (~3.97 for the sample EDA5) compared to the sample $CsPbBr_3$ (~2.27), suggesting the formation of Pb^{2+} vacancies and a hollow 3D structure. We attribute the below-nominal Br/Pb ratio in pure $CsPbBr_3$ to the presence of high surface defect density as corroborated by the short average PL decay lifetime. Energy-dispersive x-ray fluorescence (EDXRF) was also conducted to probe the relative concentrations of Pb^{2+} and Br^- in the studied samples. Br $K_{\alpha1}$ and Br $K_{\beta1}$ as well as Pb $L_{\alpha1}$ and Pb $L_{\beta1}$ lines from the four samples are shown in fig. S5A. To quantify the molar ratios between the different components, the intensity versus concentration scatterplots for the standards (fit using a linear equation) were used as calibration curves (fig. S5, B to D). The Br/Pb ratio in EDA5 obtained through EDXRF displayed a similar trend as what was observed from the XPS quantitative analysis. This confirms the formation of Pb^{2+} vacancies. The blue shift of emissions for the

$CsPbBr_3$ thin films upon the addition of $EDABr_2$ is also consistent with what was observed in hollow 3D $MASnI_3$, $MAPbI_3$, and $FASnI_3$ perovskites (32–34, 40).

Increasing the EDA^{2+} content also led to decreasing grain sizes as evidenced by the XRD peak broadening (fig. S6). The NC formation and surface defect passivation by EDA^{2+} cations resulted in considerably increased PLQEs, with the highest value recorded for EDA5 at ~81%. Overall, EDA^{2+} cations can form small crystalline domains of $CsPbBr_3$, passivate their surfaces, and penetrate the lattice to form hollow 3D structures. Further lattice expansion was observed for the sample EDA5-Na, which showed strongly blue-shifted emission as compared to the other samples. We speculate that Na^+ cations occupy interstitial sites within the perovskite structure as has been reported for alkali ions in organo-metal halide perovskites (41), because Na^+ cations are too small to create more Pb^{2+} vacancies as seen with EDA^{2+}. A slight shift to higher binding energies was also observed for Br 3d and Pb 4f core orbitals of EDA5-Na. Because of the increased lattice parameter for EDA5-Na, improved orbital overlap between Pb^{2+} and Br^- ions cannot explain the observed peak shift in the photoelectron spectra. However, the presence of interstitial defects has previously been shown to result in increased lattice parameters and photoelectron spectra shift to higher binding energies (42). Thus, we ascribe the observed lattice expansion and photoelectron spectra shift to the presence of Na^+ interstitials. Hence, EDA5-Na samples could be composed of hollow 3D structures with additional Na^+ interstitials.
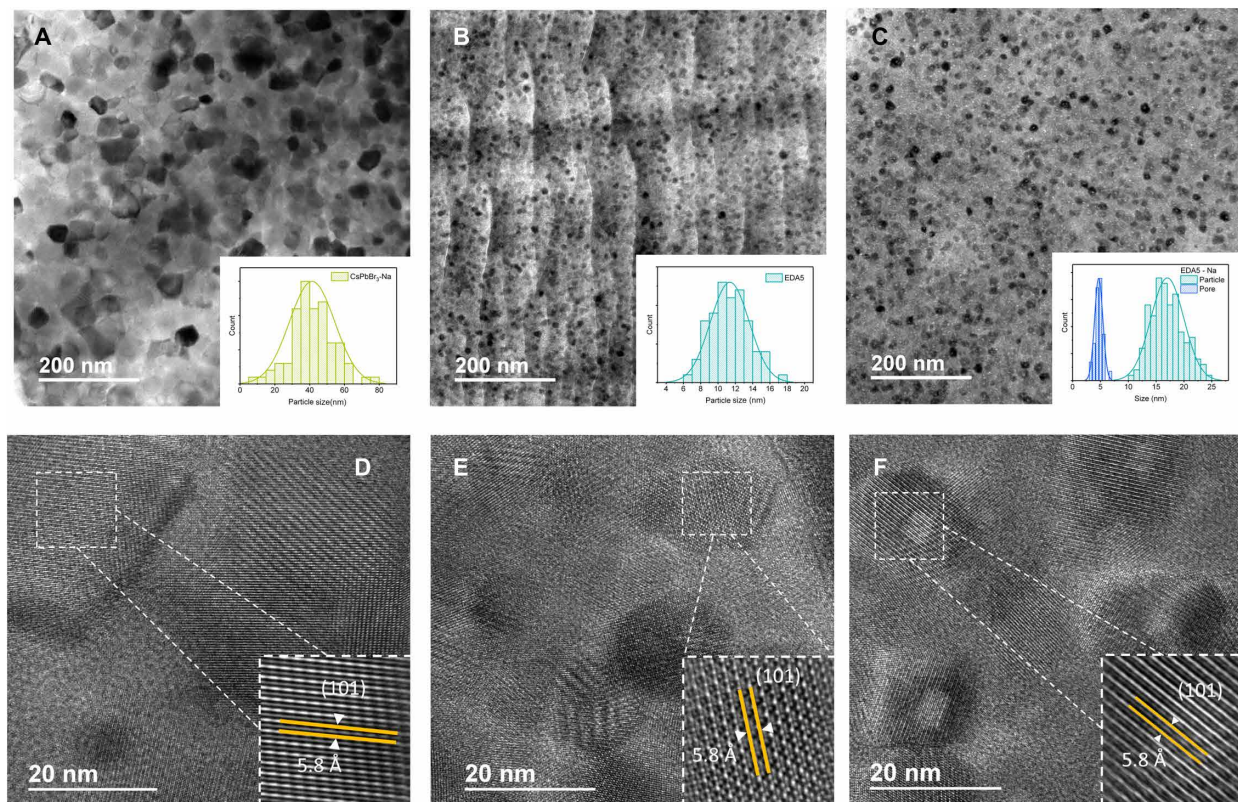
Fig. 3. TEM characterization of thin films. Transmission electron microscopy (TEM) images of (**A**) CsPbBr$_3$-Na, (**B**) EDA5, and (**C**) EDA5-Na thin films. Insets: particle and pore size distribution of NCs. High-resolution TEM (HRTEM) images of (**D**) CsPbBr$_3$-Na, (**E**) EDA5, and (**F**) EDA5-Na thin films. Inset: Simulated HRTEM images showing lattice fringes for the (101) planes.

To directly visualize the effects of the different ions on the microstructural properties of these samples, we used transmission electron microscopy (TEM) and high-resolution TEM (HRTEM) to characterize the thin films. TEM images of CsPbBr$_3$-Na, EDA5, and EDA5-Na indicate the formation of perovskite NCs (Fig. 3, A to C). Particle size distribution analysis revealed median sizes of around 40, 12, and 17 nm for CsPbBr$_3$-Na, EDA5, and EDA5-Na, respectively. As the median particle size of EDA5-Na is still much larger than the exciton bohr radius of CsPbBr$_3$ (~7 nm), blue emission from small quantum-confined CsPbBr$_3$ NCs could not be the case here. With HRTEM (Fig. 3, D to F), large pores at the center of CsPbBr$_3$ NCs with a median size of 4.25 nm were observed in EDA5-Na. The NCs with pores, or hollow NCs, could be observed throughout the whole film (fig. S7, A to D). These hollow NCs were not present in CsPbBr$_3$-Na or EDA5 (Fig. 3, D to E and fig. S8). The median shell thickness of these hollow CsPbBr$_3$ NCs was found to be 6.5 nm (inset of fig. S7C). This shell thickness is slightly larger than the grain size needed for CsPbBr$_3$ to have an emission energy of ~2.6 eV (~477 nm), i.e., ~6 nm (5). However, aside from the quantum confinement effect, the hollow 3D crystal structure of EDA5-Na will also contribute to the energy bandgap widening, as discussed above. Thus, we ascribe the observed optical bandgap widening and emission peak shift to the combined effect of quantum confinement and a hollow 3D crystal structure. These hollow nanostructures answer how the optical bandgap of CsPbBr$_3$ NCs could be tuned while the size of the NC grains was still well above the exciton bohr radius of ~7 nm.

The TEM and HRTEM images were further analyzed to confirm that the "lighter" regions were not results of intergrain voids, sample preparation artifacts, or electron-beam damage. Fast Fourier transform of TEM and scanning TEM images of monograin hollow NCs show single sets of spots, indicating the single crystalline nature of these NCs (fig. S9). Moreover, the absence of spots from multiple grains conclusively proves that the pores are not a result of intergrain voids. To exclude the TEM sample preparation as the source of the observed unique nanostructures, we conducted the TEM characterization using an alternative sample preparation technique (fig. S10). The collected TEM images were consistent with what was observed using the "scratch and sonicate" TEM sample preparation technique (experimental details in Materials and Methods), confirming that these nanostructures were not sample preparation artifacts. Moreover, the low-contrast regions in these grains do not resemble the products reported to arise from electron beam damage (Pb-rich nanoparticles) (43). In addition, TEM images taken 10 s apart for a total of 60 s show that there is little change in the microstructure of the sample, indicating that the pores are not results of electron beam damage (fig. S11).

Previous studies on hollow NCs have attributed their formation to nanoscale Kirkendall effect (25, 44), Ostwald ripening (28), galvanic replacement (27), and cation exchange (26). To gain a better understanding on the roles played by the different components during the growth of these hollow NCs, we used a combination of surface and bulk-sensitive techniques (XPS and EDX). It was found that electrons from Cs 3d$_{5/2}$, C 1 s of C—N bond, and N 1 s orbitals
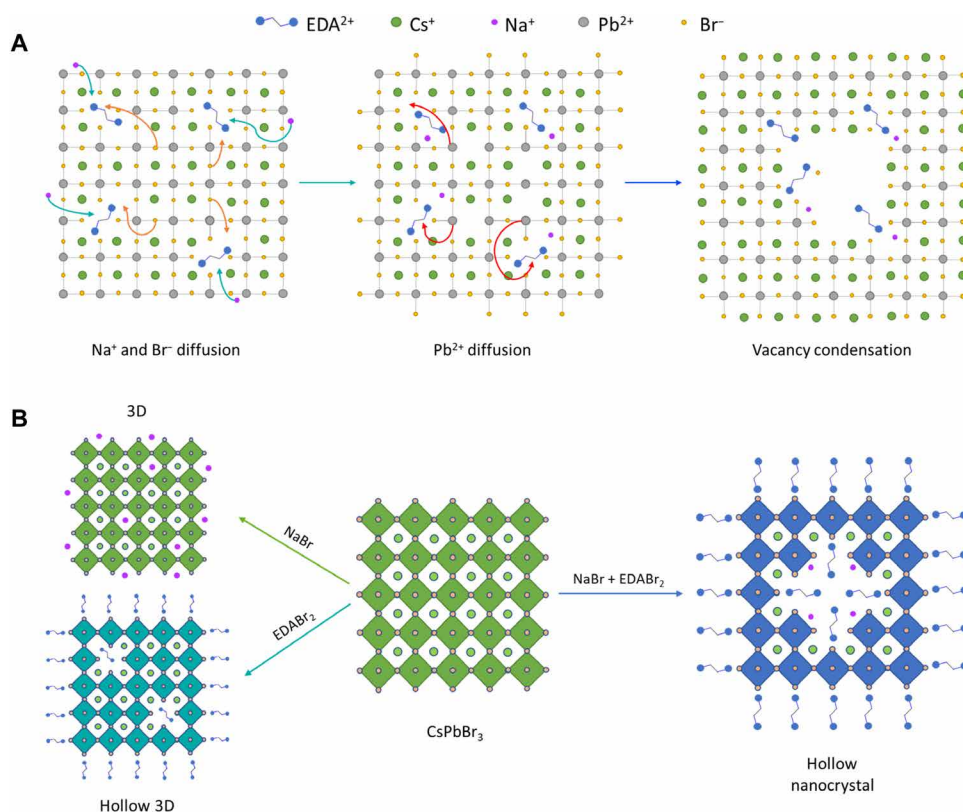
Fig. 4. Proposed formation mechanism and crystal structures. (**A**) Proposed formation mechanism of hollow $CsPbBr_3$ NCs beginning from Na^+ and Br^- diffusion from the surface to the core and vice versa, respectively, followed by Pb^{2+} diffusion via Pb^{2+} vacancies culminating in vacancy condensation (**B**) changes of the crystal structures of $CsPbBr_3$ upon the additions of NaBr, $EDABr_2$, and both NaBr and $EDABr_2$.

were detectable in XPS (fig. S12), indicating the presence of Cs^+ and EDA^{2+} ions on or near the surface. While electrons from Na 1 s orbital were readily discernable in XPS for $CsPbBr_3$-Na, they were not observed in EDA5-Na (fig. S12). In contrast, EDX spectrum of EDA5-Na confirmed the presence of Na^+ ions within the bulk (fig. S13). These results suggest that Na^+ cations were located deep in the shell or within the core of the hollow NCs. On the basis of the changes observed in the lattice, surface chemistry, and microstructure of the hollow NCs as compared to the regular NCs, we propose a formation mechanism (Fig. 4A), in which the diffusion of Na^+ ions from the surface to the core selectively draws Br^- anions from the perovskite lattice to the surface (*45*), reducing the coordination number of Pb^{2+} cations. Because undercoordinated ions generally display higher free energy compared to those that are fully coordinated, Pb^{2+} ions will likely diffuse to lattice sites with higher coordination number driven by the free-energy landscape. Although the diffusion of Pb^{2+} ions has been reported to have a high diffusion barrier of ~2.3 eV, the presence of Pb^{2+} vacancies due to the incorporation EDA^{2+} could lower this energy barrier (*46*). The diffusion of Pb^{2+} cations will be associated with vacancy migration in the opposite direction resulting in vacancy coalescence and void formation. To test the proposed mechanism, we introduced NaBr before thin-film deposition in the form of a 20-nm thin film on glass substrate. The EDA5 precursor was then deposited on top of the NaBr layer. The obtained thin film displayed a broad PL spectrum that can be deconvoluted to the spectra of EDA5 and EDA5 containing 2 mol % NaBr (fig. S14C). This result indicates that Na^+ ions can diffuse into the EDA5 thin

film to form hollow NCs. Overall, the effects of individual additives (NaBr and $EDABr_2$) and their combination on the morphological and optical properties of $CsPbBr_3$ can be summarized in Fig. 4B: the addition of only Na^+ has little to no effect on the crystalline lattice, the addition of only EDA^{2+} creates hollow 3D structures, and the addition of both Na^+ and EDA^{2+} leads to the formation of hollow perovskite NCs.

With the understanding of the roles of the different ions, we demonstrated rational control of the particle and pore sizes of $CsPbBr_3$ hollow NCs and, subsequently, their optical properties, by controlling the Na^+ and EDA^{2+} contents. The increase in Na^+ content (in the presence of EDA^{2+} 1:1 with the perovskite precursors) had no substantial effect on grain size but generally led to larger pore sizes from a median pore size of 3.2 nm for samples with 1 mol % NaBr to 4.8 nm for those containing 4 mol % of NaBr (fig. S15). This pore size increase, in turn, resulted in a narrower shell thickness and a corresponding optical bandgap widening. Conversely, increasing the EDA^{2+} concentration (in the presence of Na^+) had no obvious influence on the pore size but led to the reduction of the particle sizes. The median particle size decreased from 19 to 17 nm for the samples prepared with of 0.4 and 1.2 molar ratios of $EDABr_2$, while keeping the NaBr content constant at 3 mol % (fig. S16).

DISCUSSION
Obtaining a monograin-thick thin film could lead to further insight into the role of each component by, for instance, allowing an accurate

elemental mapping, which can conclusively show the distribution of each component. However, in situ formation of monograin-thick nanocrystalline thin film was found to be a nontrivial task. Thus, we believe that future effort in this area should be directed toward colloidal synthesis of these multicomponent hollow NCs. Freestanding NCs would not only lend a major insight into the morphology of these hollow structures but also provide a path to investigate their formation through in situ microscopy methods (*47*). Moreover, the increased degrees of freedom in colloidal synthesis of NCs may also lead to the discovery of other exotic structures.

In summary, by carefully choosing appropriate organic and alkali metal salts, light-emitting thin films containing hollow perovskite NCs can be prepared via facile solution processing. The organic cations not only penetrate the perovskite lattice to create vacancies, but also passivate the surfaces of the perovskite NCs. The small alkali metal cations can diffuse throughout the perovskite lattice to assist the formation of hollow structures with the presence of large organic cations. As a result, quantum confinement can be realized in hollow perovskite NCs with controlled pore sizes and shell thicknesses, which exhibit highly tunable emission with high PLQEs. Our work represents a groundbreaking advance in the field of metal halide perovskite NCs, from well-developed nanostructures with positive curvatures to unique hollow structures, which will stimulate exploration of other nanostructures with remarkable and unique properties. Applications of hollow perovskite NCs in various types of optoelectronic devices are envisioned in the near future.

MATERIALS AND METHODS
Materials
PbBr$_2$ (99.999%), CsBr (99%), ethylenediamine (99%), hydrobromic acid [48 weight % (wt %) in H$_2$O], NaBr (99%), and dimethyl sulfoxide (99.9%) were purchased from Sigma-Aldrich. All reagents and solvents were used without further purification unless otherwise stated.

Synthesis of C$_2$N$_2$H$_{10}$Br$_2$ (EDABr$_2$)
Ethylenediamine (1 eq) and 48 wt % hydrobromic acid (2.1 eq) were combined in ethanol at 0°C. After 30 min, white precipitate was extracted through evaporation of the solvent using a rotary evaporator. The white precipitate was washed with diethyl ether twice and was left to dry in a desiccator overnight before use. The salt was stored in a glove box.

Thin-film processing
CsBr (0.2 mmol) and PbBr$_2$ (0.2 mmol) were dissolved in 1 ml of dimethyl sulfoxide to make the perovskite precursor solution. EDABr$_2$ was added to the perovskite precursor solution in varying concentrations from 0 to 1.2 molar ratio. The Na$^+$ content in the perovskite precursor solution was controlled by varying the amount of NaBr from 0 to 4 mol %. Indium tin oxide substrates were purchased from thin-film devices (any glass substrate that does not contain sodium would work). Before use, they were sequentially cleaned by sonicating in detergent (Hellmanex III) water, deionized water, acetone, and isopropanol for 15 min and were dried in an oven overnight. The substrates (bare side) were then cleaned under UV-ozone treatment and transported into a glove box for one-step spin coating of the precursor solution at 3000 rpm for 60 s. Subsequently, the films were annealed at 100°C for 20 min.

Atomic force microscopy
AFM images were taken on a Bruker Icon scanning probe microscope in tapping mode.

PL spectroscopy
Steady-state PL was carried out using an Edinburgh FS5 steady-state spectrometer with a 150-W xenon lamp at an excitation wavelength of 365 nm. TRPL was collected using time-correlated single photon counting for 10,000 counts. Excitation was provided by an Edinburgh EPL-360 ps pulsed diode laser. The PL decay was fit using a biexponential decay curve for CsPbBr$_3$ CsPbBr$_3$-Na and EDA5 and triexponential decay function for EDA5-Na. The average lifetime was obtained from the bi- or triexponential decays according to Eq. 1.

$$\tau_{ave} = \sum \alpha_i \tau_i^2 / \sum \alpha_i \tau_i, i = 1, 2, 3 \qquad (1)$$

where τ_i represents the decay time and α_i represents the amplitude of each component.

Absorption spectrum measurements
Absorption spectra were obtained using an Agilent Technologies Cary 5000 UV-vis near-infrared spectrophotometer.

PL quantum efficiency
PLQE measurements were performed in accordance with what has been reported previously (*48*). Briefly, a Hamamatsu Quantaurus-QY Spectrometer (Model C11347-11) was equipped with a xenon lamp, an integrating sphere sample chamber, and a charge-coupled device detector. The PLQEs were calculated by the equation: $\eta QE = \frac{I_S}{E_R - E_S}$, in which I_S represents the luminescence emission spectrum of the sample, E_R is the spectrum of the excitation light for the reference (empty substrate), and E_S is the excitation spectrum for exciting the sample. The PLQE measurements were done consecutively, and a density of 0.3 mW/cm^2 at an excitation wavelength of 365 nm was used for all samples.

Powder x-ray diffraction
XRD patterns were obtained using a Siemens D500 powder diffractometer equipped with a Cu Kα x-ray source. Diffraction patterns were recorded from 5° to 40° 2θ, with a step size of 0.05° under a tube current of 30 mA and a tube voltage of 40 kV.

TEM images
Microstructural characterization was performed using TEM, on a JEOL JEM-ARM200cF at 200 kV. TEM samples were prepared by scraping thin films from substrate and dispersing the powder in a nonpolar solvent (hexane). The dispersion was sonicated for 10 min to ensure uniform distribution before dropping it on a 200-mesh Cu grid. Alternatively, Cu grids were pressed facedown on thin films prepared on polydimethylsiloxane substrates, followed by applying a single drop of 2-propanol on the Cu grid. The Cu grids were then picked up using fine tweezers before the solvent completely evaporated. TEM image analysis was performed in Gatan microscopy software suite.

X-ray photoelectron spectroscopy
XPS was conducted using a PHI 5000 series XPS equipped with a dual anode x-ray source. For our purpose, Al Kα radiation with a

photon energy of 1486.6 eV at a take-off angle of 45° and a pass energy of 35.75 eV were used. Charge compensation was performed using adventitious C 1 s peak (284.6 eV). Spectra background was fit and subtracted using an integrated Shirley function. XPS curves were deconvoluted using a Voight peak function for metal core electron spectra and Gaussian peak functions for the rest.

Energy-dispersive x-ray fluorescence
EDXRF was performed using a Panalytical Epsilon 3 spectrometer equipped with a rhodium x-ray tube and a silicon drift detector.

SUPPLEMENTARY MATERIALS
Supplementary material for this article is available at http://advances.sciencemag.org/cgi/content/full/6/17/eaaz5961/DC1

REFERENCES AND NOTES
1. M. V. Kovalenko, L. Protesescu, M. I. Bodnarchuk, Properties and potential optoelectronic applications of lead halide perovskite nanocrystals. *Science* **358**, 745–750 (2017).
2. X. He, Y. Qiu, S. Yang, Fully-inorganic trihalide perovskite nanocrystals: A new research frontier of optoelectronic materials. *Adv. Mater.* **29**, 1700775 (2017).
3. J. Shamsi, A. S. Urban, M. Imran, L. De Trizio, L. Manna, Metal halide perovskite nanocrystals: Synthesis, post-synthesis modifications, and their optical properties. *Chem. Rev.* **119**, 3296–3348 (2019).
4. J. Huang, M. Lai, J. Lin, P. Yang, Rich chemistry in inorganic halide perovskite nanostructures. *Adv. Mater.* **30**, 1802856 (2018).
5. L. Protesescu, S. Yakunin, M. I. Bodnarchuk, F. Krieg, R. Caputo, C. H. Hendon, R. X. Yang, A. Walsh, M. V. Kovalenko, Nanocrystals of cesium lead halide perovskites (CsPbX₃, X = Cl, Br, and I): Novel optoelectronic materials showing bright emission with wide color gamut. *Nano Lett.* **15**, 3692–3696 (2015).
6. I. Levchuk, A. Osvet, X. Tang, M. Brandl, J. D. Perea, F. Hoegl, G. J. Matt, R. Hock, M. Batentschuk, C. J. Brabec, Brightly luminescent and color-tunable formamidinium lead halide perovskite FAPbX₃ (X = Cl, Br, I) colloidal nanocrystals. *Nano Lett.* **17**, 2765–2770 (2017).
7. D. Amgar, A. Stern, D. Rotem, D. Porath, L. Etgar, Tunable length and optical properties of CsPbX₃ (X = Cl, Br, I) nanowires with a few unit cells. *Nano Lett.* **17**, 1007–1013 (2017).
8. A. Pan, B. He, X. Fan, Z. Liu, J. J. Urban, A. P. Alivisatos, L. He, Y. Liu, Insight into the ligand-mediated synthesis of colloidal CsPbBr₃ perovskite nanocrystals: The role of organic acid, base, and cesium precursors. *ACS Nano* **10**, 7943–7954 (2016).
9. D. Zhang, Y. Yu, Y. Bekenstein, A. B. Wong, A. P. Alivisatos, P. Yang, Ultrathin colloidal cesium lead halide perovskite nanowires. *J. Am. Chem. Soc.* **138**, 13155–13158 (2016).
10. D. Zhang, Y. Yang, Y. Bekenstein, Y. Yu, N. A. Gibson, A. B. Wong, S. W. Eaton, N. Kornienko, Q. Kong, M. Lai, A. P. Alivisatos, S. R. Leone, P. Yang, Synthesis of composition tunable and highly luminescent cesium lead halide nanowires through anion-exchange reactions. *J. Am. Chem. Soc.* **138**, 7236–7239 (2016).
11. D. Zhang, S. W. Eaton, Y. Yu, L. Dou, P. Yang, Solution-phase synthesis of cesium lead halide perovskite nanowires. *J. Am. Chem. Soc.* **137**, 9230–9233 (2015).
12. Y. Bekenstein, B. A. Koscher, S. W. Eaton, P. D. Yang, A. P. Alivisatos, Highly luminescent colloidal nanoplates of perovskite cesium lead halide and their oriented assemblies. *J. Am. Chem. Soc.* **137**, 16008–16011 (2015).
13. Q. A. Akkerman, V. D'Innocenzo, S. Accornero, A. Scarpellini, A. Petrozza, M. Prato, L. Manna, Tuning the optical properties of cesium lead halide perovskite nanocrystals by anion exchange reactions. *J. Am. Chem. Soc.* **137**, 10276–10281 (2015).
14. Z. Yuan, Y. Shu, Y. Xin, B. Ma, Highly luminescent nanoscale quasi-2D layered lead bromide perovskites with tunable emissions. *Chem. Commun.* **52**, 3887–3890 (2016).
15. Z. Li, L. Kong, S. Huang, L. Li, Highly luminescent and ultrastable CsPbBr₃ perovskite quantum dots incorporated into a silica/alumina monolith. *Angew. Chem. Int. Ed. Eng.* **56**, 8134–8138 (2017).
16. V. Malgras, J. Henzie, T. Takei, Y. Yamauchi, Stable blue luminescent CsPbBr₃ perovskite nanocrystals confined in mesoporous thin films. *Angew. Chem. Int. Ed.* **57**, 8881–8885 (2018).
17. B. J. Bohn, Y. Tong, M. Gramlich, M. L. Lai, M. Döblinger, K. Wang, R. L. Z. Hoye, P. Müller-Buschbaum, S. D. Stranks, A. S. Urban, L. Polavarapu, J. Feldmann, Boosting tunable blue luminescence of halide perovskite nanoplatelets through postsynthetic surface trap repair. *Nano Lett.* **18**, 5231–5238 (2018).
18. Y. Xu, Q. Zhang, L. Lv, W. Han, G. Wu, D. Yang, A. Dong, Synthesis of ultrasmall CsPbBr₃ nanoclusters and their transformation to highly deep-blue-emitting nanoribbons at room temperature. *Nanoscale* **9**, 17248–17253 (2017).
19. H. Huang, M. Liu, J. Li, L. Luo, J. Zhao, Z. Luo, X. Wang, Z. Ye, H. He, J. Zeng, Atomically thin cesium lead bromide perovskite quantum wires with high luminescence. *Nanoscale* **9**, 104–108 (2017).
20. Y. Wu, C. Wei, X. Li, Y. Li, S. Qiu, W. Shen, B. Cai, Z. Sun, D. Yang, Z. Deng, H. Zeng, In situ passivation of PbBr₆⁴⁻ octahedra toward blue luminescent CsPbBr₃ nanoplatelets with near 100% absolute quantum yield. *ACS Energy Lett.* **3**, 2030–2037 (2018).
21. A. Dutta, S. K. Dutta, S. Das Adhikari, N. Pradhan, Tuning the size of CsPbBr₃ nanocrystals: All at one constant temperature. *ACS Energy Lett.* **3**, 329–334 (2018).
22. G. Almeida, L. Goldoni, Q. Akkerman, Z. Dang, A. H. Khan, S. Marras, I. Moreels, L. Manna, Role of acid–base equilibria in the size, shape, and phase control of cesium lead bromide nanocrystals. *ACS Nano* **12**, 1704–1711 (2018).
23. Y. Dong, T. Qiao, D. Kim, D. Parobek, D. Rossi, D. H. Son, Precise control of quantum confinement in cesium lead halide perovskite quantum dots via thermodynamic equilibrium. *Nano Lett.* **18**, 3716–3722 (2018).
24. Y.-H. Kim, C. Wolf, Y. T. Kim, H. Cho, W. Kwon, S. Do, A. Sadhanala, C. G. Park, S. W. Rhee, S. H. Im, R. H. Friend, T. W. Lee, Highly efficient light-emitting diodes of colloidal metal–halide perovskite nanocrystals beyond quantum size. *ACS Nano* **11**, 6586–6593 (2017).
25. Y. D. Yin, R. M. Rioux, C. K. Erdonmez, S. Hughes, G. A. Somorjai, A. P. Alivisatos, Formation of hollow nanocrystals through the nanoscale Kirkendall effect. *Science* **304**, 711–714 (2004).
26. D. H. Son, S. M. Hughes, Y. Yin, A. P. Alivisatos, Cation exchange reactions in ionic nanocrystals. *Science* **306**, 1009–1012 (2004).
27. M. H. Oh, T. Yu, S. H. Yu, B. Lim, K. T. Ko, M. G. Willinger, D. H. Seo, B. H. Kim, M. G. Cho, J. H. Park, K. Kang, Y. E. Sung, N. Pinna, T. Hyeon, Galvanic replacement reactions in metal oxide nanocrystals. *Science* **340**, 964–968 (2013).
28. X. W. Lou, Y. Wang, C. L. Yuan, J. Y. Lee, L. A. Archer, Template-free synthesis of SnO₂ hollow nanostructures with high lithium storage capacity. *Adv. Mater.* **18**, 2325–2329 (2006).
29. Y. Yin, C. Erdonmez, S. Aloni, A. P. Alivisatos, Faceting of nanocrystals during chemical transformation: From solid silver spheres to hollow gold octahedra. *J. Am. Chem. Soc.* **128**, 12671–12673 (2006).
30. S. J. Lee, J. H. Park, B. R. Lee, E. D. Jung, J. C. Yu, D. Di Nuzzo, R. H. Friend, M. H. Song, Amine-based passivating materials for enhanced optical properties and performance of organic inorganic perovskites in light-emitting diodes. *J. Phys. Chem. Lett.* **8**, 1784–1792 (2017).
31. M. Abdi-Jalebi, M. Pazoki, B. Philippe, M. I. Dar, M. Alsari, A. Sadhanala, G. Divitini, R. Imani, S. Lilliu, J. Kullgren, H. Rensmo, M. Grätzel, R. H. Friend, Dedoping of lead halide perovskites incorporating monovalent cations. *ACS Nano* **12**, 7301–7311 (2018).
32. I. Spanopoulos, W. Ke, C. C. Stoumpos, E. C. Schueller, O. Y. Kontsevoi, R. Seshadri, M. G. Kanatzidis, Unraveling the chemical nature of the 3D "hollow" hybrid halide perovskites. *J. Am. Chem. Soc.* **140**, 5728–5742 (2018).
33. W. J. Ke, C. C. Stoumpos, I. Spanopoulos, L. Mao, M. Chen, M. R. Wasielewski, M. G. Kanatzidis, Efficient lead-free solar cells based on hollow {en}MASnI₃ perovskites. *J. Am. Chem. Soc.* **139**, 14800–14806 (2017).
34. W. J. Ke, C. C. Stoumpos, M. Zhu, L. Mao, I. Spanopoulos, J. Liu, O. Y. Kontsevoi, M. Chen, D. Sarma, Y. Zhang, M. R. Wasielewski, M. G. Kanatzidis, Enhanced photovoltaic performance and stability with a new type of hollow 3D perovskite {en}FASnI₃. *Sci. Adv.* **3**, e1701293 (2017).
35. J. F. Lu, L. Jiang, W. Li, F. Li, N. K. Pai, A. D. Scully, C.-M. Tsai, U. Bach, A. N. Simonov, Y.-B. Cheng, L. Spiccia, Diammonium and monoammonium mixed-organic-cation perovskites for high performance solar cells with improved stability. *Adv. Energy Mater.* **7**, 1700444 (2017).
36. M. Daub, H. Hillebrecht, Tailoring the band gap in 3D hybrid perovskites by substitution of the organic cations: (CH₃NH₃)₁₋₂ᵧ(NH₃(CH2)₂NH₃)₂ᵧPb₁₋ᵧI₃ (0≤y≤0.25). *Chem. Eur. J.* **24**, 9075–9082 (2018).
37. R. Prasanna, A. Gold-Parker, T. Leijtens, B. Conings, A. Babayigit, H. G. Boyen, M. F. Toney, M. D. McGehee, Band gap tuning via lattice contraction and octahedral tilting in perovskite materials for photovoltaics. *J. Am. Chem. Soc.* **139**, 11117–11124 (2017).
38. J. K. Nam, S. U. Chai, W. Cha, Y. J. Choi, W. Kim, M. S. Jung, J. Kwon, D. Kim, J. H. Park, Potassium incorporation for enhanced performance and stability of fully inorganic cesium lead halide perovskite solar cells. *Nano Lett.* **17**, 2028–2033 (2017).
39. M. Liu, G. Zhong, Y. Yin, J. Miao, K. Li, C. Wang, X. Xu, C. Shen, H. Meng, Aluminum-doped cesium lead bromide perovskite nanocrystals with stable blue photoluminescence used for display backlight. *Adv. Sci.* **4**, (2017).
40. Z. Chen, X. Zheng, F. Yao, J. Ma, C. Tao, G. Fang, Methylammonium, formamidinium and ethylenediamine mixed triple-cation perovskite solar cells with high efficiency and remarkable stability. *J. Mater. Chem. A* **6**, 17625–17632 (2018).
41. J. Cao, S. X. Tao, P. A. Bobbert, C.-P. Wong, N. Zhao, Interstitial occupancy by extrinsic alkali cations in perovskites and its impact on ion migration. *Adv. Mater.* **30**, 1707350 (2018).
42. T. Nishimatsu, M. Sluiter, H. Mizuseki, Y. Kawazoe, Y. Sato, M. Miyata, M. Uehara, Prediction of XPS spectra of silicon self-interstitials with the all-electron mixed-basis method. *Phys. B Condens. Matter* **340**, 570–574 (2003).
43. Z. Y. Dang, J. Shamsi, F. Palazon, M. Imran, Q. A. Akkerman, S. Park, G. Bertoni, M. Prato, R. Brescia, L. Manna, In situ transmission electron microscopy study of electron

beam-induced transformations in colloidal cesium lead halide perovskite nanocrystals. *ACS Nano* **11**, 2124–2132 (2017).

44. W. Wang, M. Dahl, Y. Yin, Hollow nanocrystals through the nanoscale Kirkendall effect. *Chem. Mater.* **25**, 1179–1189 (2013).

45. M. Abdi-Jalebi, Z. Andaji-Garmaroudi, S. Cacovich, C. Stavrakas, B. Philippe, J. M. Richter, M. Alsari, E. P. Booker, E. M. Hutter, A. J. Pearson, S. Lilliu, T. J. Savenije, H. Rensmo, G. Divitini, C. Ducati, R. H. Friend, S. D. Stranks, Maximizing and stabilizing luminescence from halide perovskites with potassium passivation. *Nature* **555**, 497–501 (2018).

46. A. Walsh, S. D. Stranks, Taking control of ion transport in halide perovskite solar cells. *ACS Energy Lett.* **3**, 1983–1990 (2018).

47. Y. Zhou, O. S. Game, S. Pang, N. P. Padture, Microstructures of organometal trihalide perovskites for solar cells: Their evolution from solutions and characterization. *J. Phys. Chem. Lett.* **6**, 4827–4839 (2015).

48. J. C. deMello, H. F. Wittmann, R. H. Friend, An improved experimental determination of external photoluminescence quantum efficiency. *Adv. Mater.* **9**, 230–232 (1997).

Citation: M. Worku, Y. Tian, C. Zhou, H. Lin, M. Chaaban, L.-j. Xu, Q. He, D. Beery, Y. Zhou, X. Lin, Y.-f. Su, Y. Xin, B. Ma, Hollow metal halide perovskite nanocrystals with efficient blue emissions. *Sci. Adv.* **6**, eaaz5961 (2020).

Science Advances

Hollow metal halide perovskite nanocrystals with efficient blue emissions

Michael Worku, Yu Tian, Chenkun Zhou, Haoran Lin, Maya Chaaban, Liang-jin Xu, Qingquan He, Drake Beery, Yan Zhou, Xinsong Lin, Yi-feng Su, Yan Xin and Biwu Ma

ARTICLE TOOLS	http://advances.sciencemag.org/content/6/17/eaaz5961
SUPPLEMENTARY MATERIALS	http://advances.sciencemag.org/content/suppl/2020/04/20/6.17.eaaz5961.DC1
REFERENCES	This article cites 47 articles, 5 of which you can access for free http://advances.sciencemag.org/content/6/17/eaaz5961#BIBL
PERMISSIONS	http://www.sciencemag.org/help/reprints-and-permissions

Use of this article is subject to the Terms of Service